Measurement of process dynamics through coaxially aligned high speed near-infrared imaging in laser powder bed fusion additive manufacturing

Jason C. Fox*[a], Brandon M. Lane[a], Ho Yeung[a]

[a]National Institute of Standards and Technology, 100 Bureau Drive, Gaithersburg, MD, USA 20899

ABSTRACT

For process stability in laser powder bed fusion (LPBF) additive manufacturing (AM), control of melt pool dimensions is imperative. In order to control melt pool dimensions in real time, sampling frequencies in excess of 10 kHz may be required, which presents a challenge for many thermal and optical monitoring systems. The National Institute of Standards and Technology (NIST) is currently developing the Additive Manufacturing Metrology Testbed (AMMT), which replicates a metal based laser powder bed fusion AM process while providing open architecture for control, sensing, and calibration sources. The system is outfitted with a coaxially aligned, near-infrared (NIR) high speed melt pool monitoring (MPM) system. Similar monitoring systems are incorporated into LPBF research testbeds, and appearing on commercial machines, but at lower available frame rates, which may limit observation of higher frequency events such as spatter or size fluctuations. This paper presents an investigation of the coaxial imaging systems of the AMMT to capture the process dynamics, and quantify the effects of dynamic fluctuations on melt pool size measurements. Analysis is carried out on a baseline experiment with no powder material added, melt pool size measurements collected in-situ are compared to ex-situ measurements, and results are discussed in terms of temporal bandwidth. Findings will show that, even at the frame rate and resolution presented, challenges in relating in-situ video signals to the ex-situ measurement analysis remain.

Keywords: Additive Manufacturing, Laser Powder Bed Fusion, Melt Pool Monitoring, Control

1. INTRODUCTION

Laser powder bed fusion (LPBF) is an additive manufacturing (AM) technique which utilizes a high power, focused laser to selectively melt layers of metal powder, which ultimately form a near fully-dense, three-dimensional structure. Multiple deficiencies plague this process, such as defects (porosity, residual stress, anisotropic microstructure, etc.) and overall part-to-part variability which inhibits part qualification and certification for aerospace or medical applications [1]. In-situ process monitoring is a suite of tools with high potential to address the problem of qualification and certification. Process monitoring enables a 'certify as you build' concept [2], in which data collected from sensors and instruments during the build process can provide sufficient part quality information so that the need for post-process destructive or non-destructive evaluation (NDE) is significantly reduced [3].

Process monitoring for LPBF is still largely in a research and development phase; however, several monitoring technologies are being implemented by LPBF machine manufacturers or third party developers [4,5]. Many of these techniques focus on process signatures stemming from the laser-induced melt pool. One melt pool monitoring (MPM) technique, now appearing on multiple commercial LPBF systems, utilizes a high-speed camera placed in the optical path co-axially aligned with the laser. This co-axial MPM method utilizes either a beam-splitter or spectrally selective mirror to separate out the laser wavelength from radiation stemming from the incandescing melt pool source. This creates a nominally stationary image of the melt pool on the imaging detector. Berumen et al. provided one of the first analyses of the spatial and temporal requirements of a co-axial MPM system as a function of melt pool size and scanning speed [6]. In their example, they surmised that 15 pixels were sufficient magnification (e.g., 10 μm/pixel to observe a 150 μm melt pool) and one frame per melt pool width was sufficient speed (e.g., 6 666 frames/s to capture a 150 μm wide melt pool scanning at 1 m/s) to capture melt pool signatures in a co-axial MPM system.

Certain commercial entities, equipment, or materials may be identified in this document in order to describe an experimental procedure or concept adequately. Such identification is not intended to imply recommendation or endorsement by the National Institute of Standards and Technology, nor is it intended to imply that the entities, materials, or equipment are necessarily the best available for the purpose.

*Jason.Fox@NIST.gov; 1 (301) 975-2171

Ultimately, signatures captured from a co-axial MPM system are intended to correlate to some physical qualities of the melted scan tracks, and ultimately the quality of the final part composed of millions of these tracks. Conversely, high resolution ex-situ measurements of scan tracks and their surface morphology may be used to qualify observations made with a co-axial MPM system and provide physical context for the captured images. In the work presented here, we compare directly ex-situ scan track measurements (width and height variation) with high speed co-axial MPM. Temporal resolution (defined by the camera frame rate and integration time) is set nearly an order of magnitude higher than the requirements outlined by Berumen at al. (30 000 frames/s). This allows melt pool size fluctuations, or other phenomena such as particle ejecta, to be better captured, which otherwise may affect MPM spatial (size) signatures. Optical magnification of the system utilized in this work provides 15 μm/pixel imaging, which is on par with the aforementioned requirements. However, it should be noted that the projected pixel size (μm/pixel) is not the definition of the spatial resolution, which is affected by optical blur.

With these aspects in mind, the purpose of this paper is to understand the relationship between signatures captured from a co-axial MPM and the resultant scan track. To accomplish this goal, a methodology for the analysis of co-axial high speed NIR MPM video is presented along with detailed ex-situ measurement of the solidified scan track. Analysis is performed on a single scan track as a baseline experiment to maintain focus on the development of the methodology. While analysis techniques of the MPM signal are purposefully kept to simple mathematical operations, they are shown to be capable of highlighting variations due to key events, such as material ejecta. Finally, the relationship between the MPM signal and resultant scan track is discussed.

2. METHODOLOGY

Experiments were performed in the Additive Manufacturing Metrology Testbed (AMMT) prototyping system [7,8], shown in Figure 1. The system uses a 500 W multimode Yb fiber laser at 1070 nm wavelength, which is delivered through two XY galvanometer scan mirrors, and focused onto a horizontal build platform within an inert gas chamber. This creates a nominally 100 μm full width at half maximum (FWHM) spot at the laser focus. Light emitted from the laser-heated region is passed back co-axially with the laser beam path, but transmitted through a beam splitter which reflects off the 1070 nm laser wavelength, and transmits wavelengths from 950 nm to 400 nm. This transmitted light is then focused with an imaging lens and passed through an 850 nm filter (40 nm bandpass) directly onto the Silicon-based complementary metal oxide semiconductor (CMOS) detector of a vertically-mounted high speed camera, shown in Figure 2. Pixel pitch on the detector is 20 μm/pixel, and magnification of the imaging lens equates this to approximately 12 μm/pixel on the image plane ($\approx$ 1.3x). The high-speed camera is capable of 6400 frames/s at full 1024 pixel x 1024 pixel window, however a sub-window of 256 pixel x 256 pixel was set to achieve higher frame rate of 30 000 frames/s. The camera was also set with a 31.62 μs exposure time; which is close to one full frame period (inverse of the frame rate).
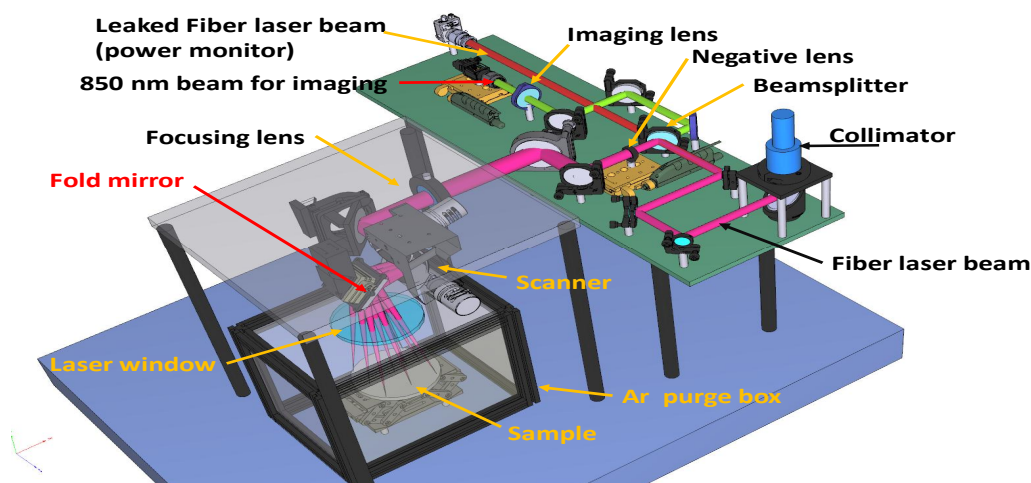

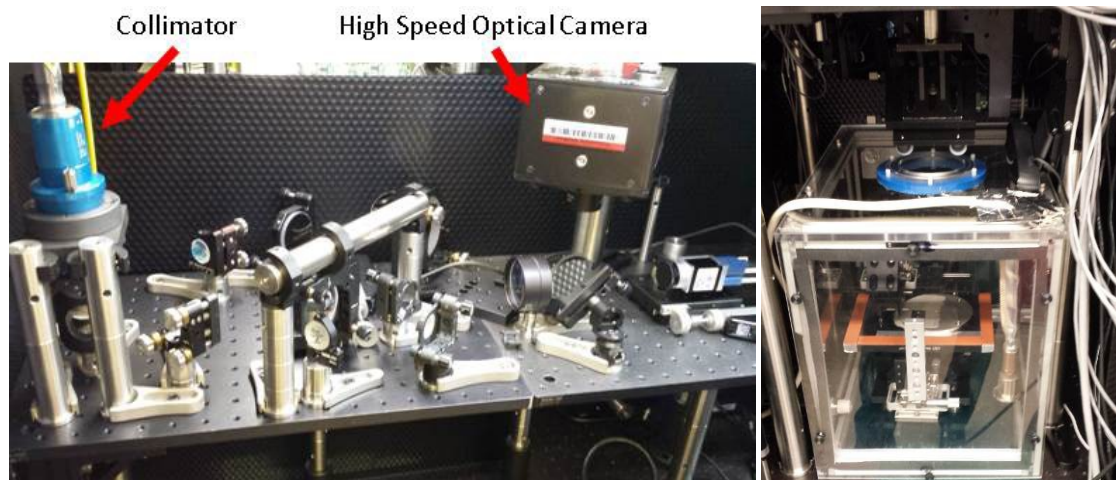Figure 1. Schematic of the AMMT prototype system [8].

Figure 2. Laser collimator, optical components, and high speed optical system (left). Fold mirror, purge box, and sample positioning system (right).

The data taken from the camera is converted to an 8-bit digital signal, with dynamic range from 0 to 255 digital levels. An example frame from the high-speed camera can be seen in Figure 3, which was taken during a scan on a 17-4 stainless steel plate. In this image, much of the center portion of the melt pool is saturated, and areas far from the melt pool are at the noise floor of the camera. This is a result of the exceedingly high temperatures and temperature gradients on the melt pool surface. The exposure time of the camera was adjusted until the approximated melt pool width (≈ 100 μm) was achieved in the camera image when masked with a digital level threshold of 128, or roughly the center of the dynamic range. From these images, further analysis can be performed to develop more exact relationships to ex-situ scan track measurements.
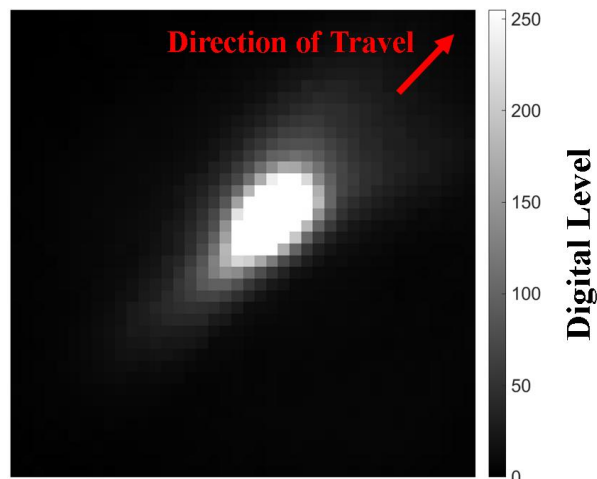

Figure 3. Single frame from the coaxially aligned high-speed imaging system.

While more advanced techniques for analysis of the video data exist, the number of computations required for those methods may be prohibitive for digital processing and real-time feedback control. As such, the focus of the data analysis will be on simple mathematical operations that can be performed very quickly. One method for analysis of the videos is to perform a conversion to binary using a pre-defined threshold. Area measurements can then be made by counting the number of pixels above the threshold. Width measurements can also be performed on the binary video by counting the maximum number of registered pixels in a line perpendicular to the direction of travel. Examples of how different thresholds change the image from Figure 3, as well as area and width measurements on the resulting binary image, can

be seen in Figure 4. Note that these threshold levels are chosen less for a calibrated measurement and more for the identification of features and anomalies, which is discussed later in the paper.
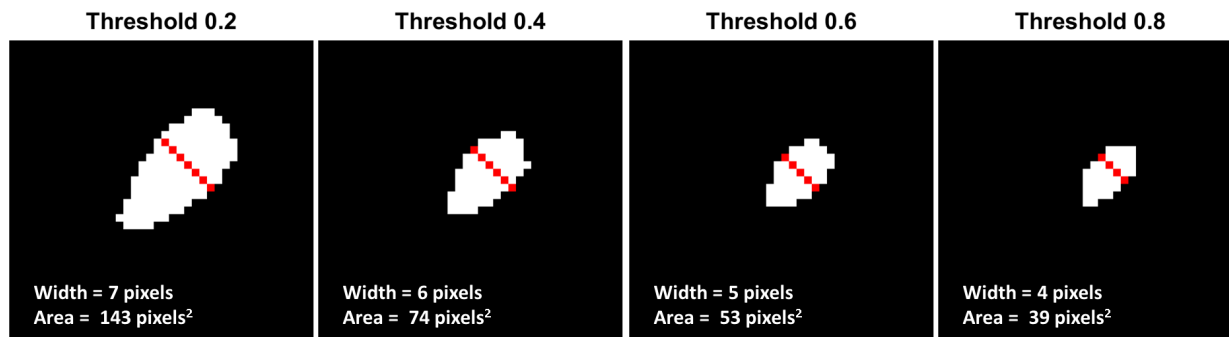

| Threshold 0.2 | Threshold 0.4 | Threshold 0.6 | Threshold 0.8 |

Width = 7 pixels
Area = 143 pixels²

Width = 6 pixels
Area = 74 pixels²

Width = 5 pixels
Area = 53 pixels²

Width = 4 pixels
Area = 39 pixels²

Figure 4. Examples of conversion to binary using different threshold levels. Values for the threshold are from 0 to 1, where 0 would include any pixel with a value greater than 0 in the binary image and 1 would not include any pixels. Area is calculated as the sum of red and white pixels. Width is calculated as the sum of red pixels.

Ex-situ analysis of the laser scan tracks from the experiment was performed via optical microscope for measurement of the scan track width and laser confocal microscope with a 405 nm source for measurement of the scan track height. The optical images were taken using a 50x objective and stitched using the microscope manufacturer's built-in stitching algorithm. Topographic measurements were taken using 20x enhanced contrast (EC) Epiplan-Apochromatic objective with a 0.6 numerical aperture and 0.5x tube lens, resulting in 0.62 µm per pixel. Topographic data was only corrected for tilt and piston (i.e., adjusted so that the average height of the surface is set to zero) and no other filtering was applied.

Width measurement can also be performed using the optical images. Often in literature, width measurements are reported as a single measurement or average with little or no information as to the variability of the width provided. To correlate the MPM signal to features in the resultant scan track, however, a detailed record of the width along the full length of the scan track is required. As such, width measurements were performed by manually tracing the edges of the scan track in the optical images and using commercially available analysis software to determine the distance between the traces. An example of this measurement can be seen in Figure 5.
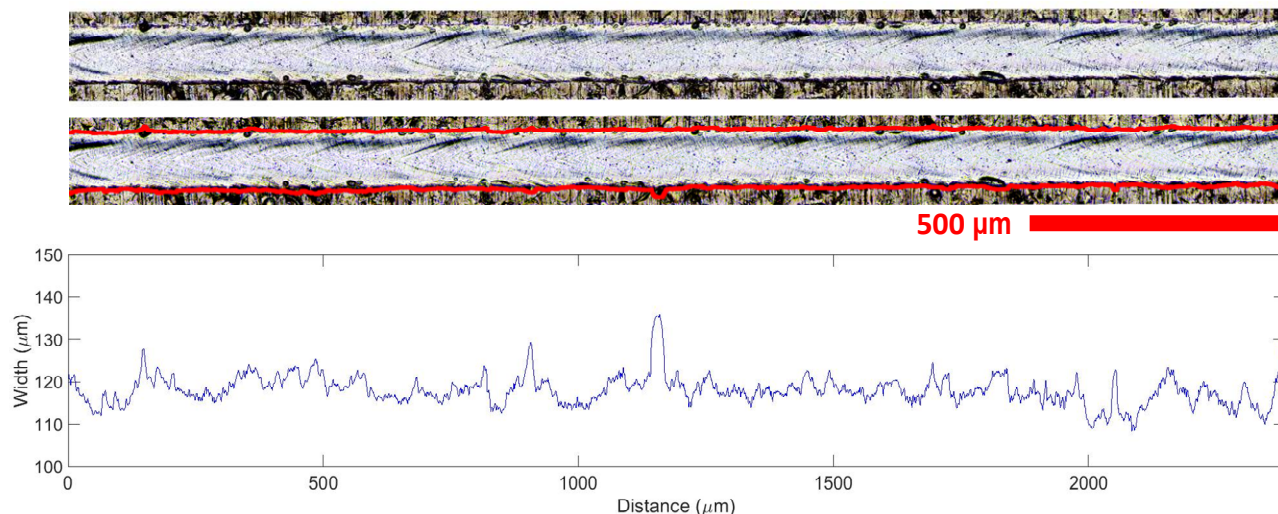

Figure 5. Center image of the track (top), trace of the track highlighted in red (center), and measured width (bottom). The traces in this figure have been widened for visibility and may not represent the true position used in the analysis. Measurement error is estimated to be ±2 µm based the ability to accurately determine the edge of the track accounting for the focus of the image at the edge of the track and size of pixels.

3. EXPERIMENTAL RESULTS

For this analysis, a single scan track using a source power of 195 W and velocity of 800 mm/s on 17-4 stainless steel was deposited with no powder material added (i.e., beam on plate only). This experiment will serve as a baseline measurement for development of appropriate methodologies. Prior work by NIST has found that higher variance in melt pool size and greater dynamics in MPM systems can be expected when scanning over powder material and that stronger understanding of the process and analysis methodologies can be achieved through preliminary experiments without the added layer of powder material [9,10]. Therefore, while additional scan tracks at this and other power and velocity combinations were performed with and without the layer of powder material, analysis of those results will be reserved for future publication and this paper will focus only on the development of the methodology using data from the scan track without any added powder material at the aforementioned power and velocity.

3.1 In-Situ Melt Pool Monitoring Results

The pixel count from various thresholds, previously described in Figure 4, for each frame of the video can be seen in Figure 6. This method, in theory, should provide a qualitative understanding as to changes in melt pool (i.e., increases and decreases in size). However, it should be noted that this is only indicative of the apparent melt pool size. True melt pool size based on MPM imaging requires calibration of the camera, which has not yet been performed. Additionally, the apparent melt pool size in the image stems from the incandescent light generated by the hot surface, which depends on the temperature and emissivity of the surface, both of which vary spatially. In addition, gain, gamma, exposure time, etc. affect the apparent melt pool size in the image [11].
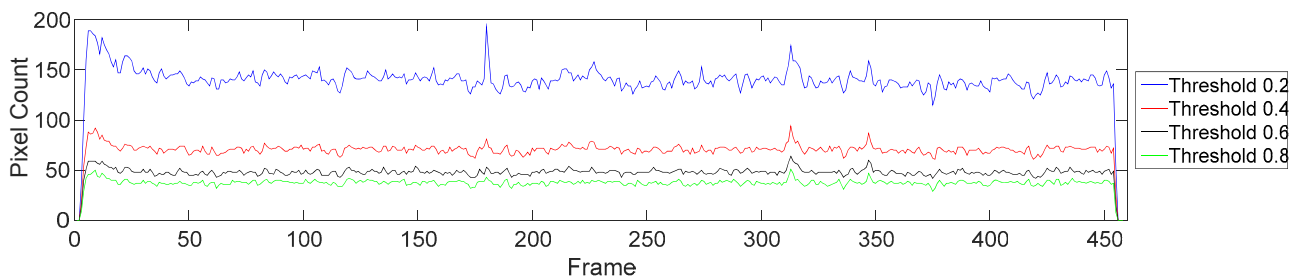

Figure 6. Example pixel count of melt pool size after conversion to binary using different threshold levels. Values for the threshold are from 0 to 1, where 0 would include any pixel with a value greater than 0 in the binary image, 0.5 would only include pixels with a value in the top 50 %, and 1 would not include any pixels.

A threshold level of 0.3 leads to approximately 6 pixels in the width of the melt pool and a threshold level of 0.2 leads to approximately 7 pixels in the width of the melt pool. With a 15 μm pixel size and using a center to center distance across the pixels, this corresponds to 106 μm to 127 μm, respectively, which is in accordance with the expected scan track width. The maximum width of the melt pool using a threshold level of 0.2 for the entire video can be seen in Figure 7.
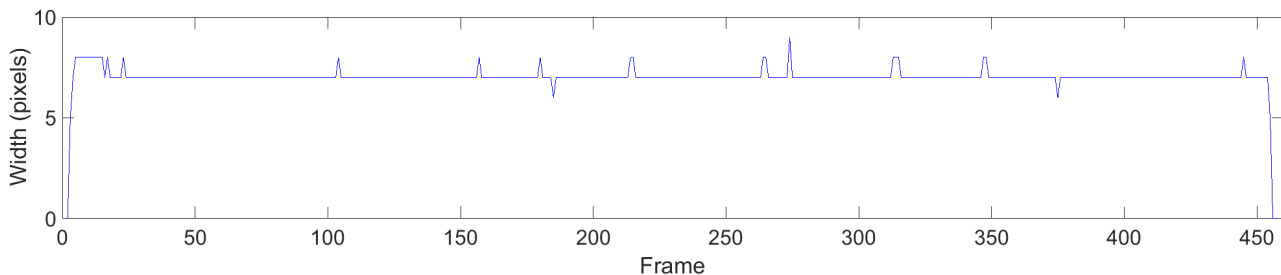

Figure 7. Maximum width of the melt pool for a threshold level of 0.2.

3.2 Ex-Situ Measurement Results

Images of the resultant scan track, taken via optical microscope, are shown in Figure 8.
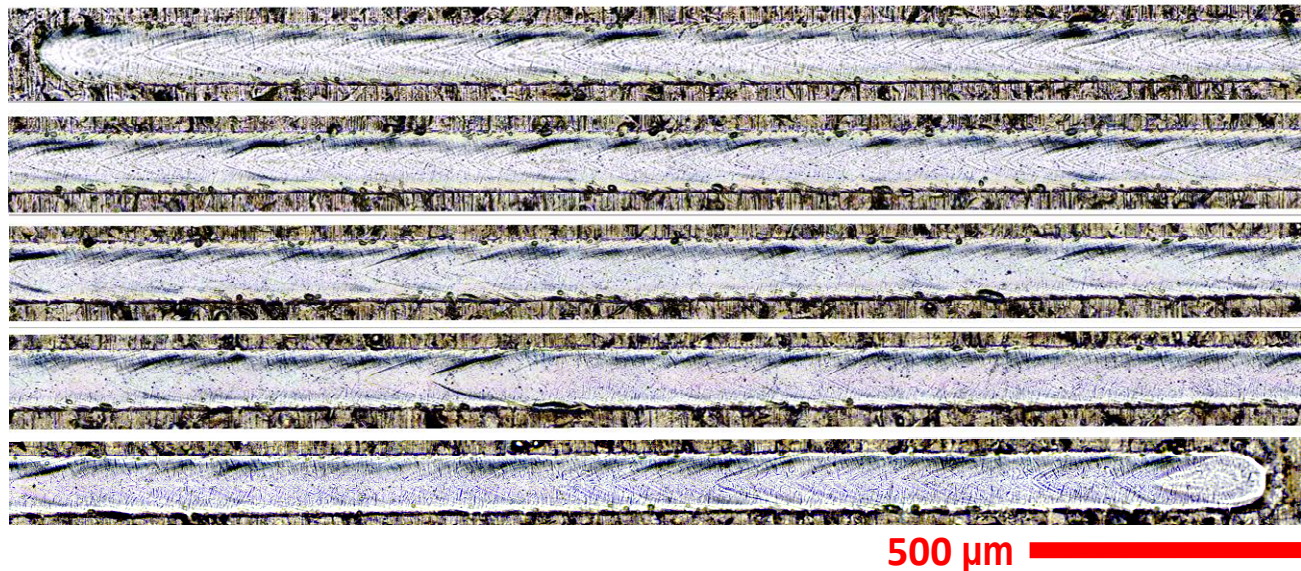

Figure 8. Optical images of the scan track. Direction of scan is from left to right. For better visibility, the image has been split into five sections, with the top being the start of the track and the bottom being the end.

Measurement of the scan track width using the method previously described in the Methodology section can be seen in Figure 9. The average can be calculated from this measurement after removing the first and last millimeter to minimize end effects from the laser turning on and off at the start and end of the scan track. The result is an average width of (117.9 ± 4.3) µm, where the number following the $\pm$ is one standard deviation, which is on par with expectations and the width measurements from the high-speed video, detailed in the previous section. Note that the length of the track is shorter than the expected 12 mm, which may be a result of errors incurred by the stitching algorithm of the microscope.
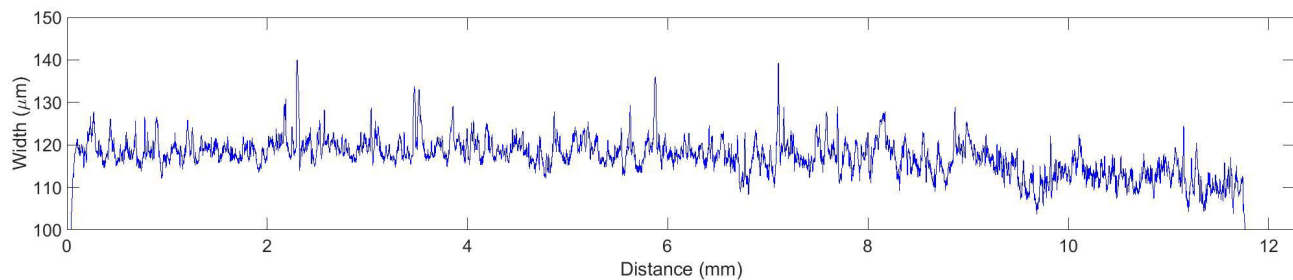

Figure 9. Measured width of the full scan track using the optical images shown in Figure 8.

Height data was also acquired using the laser confocal microscope described in the Methodology section to determine if evidence can be found relating the in-situ camera data to the solidified melt track. A height profile, which was taken down the center of the scan track and will be used in later comparisons, can be seen in Figure 10.
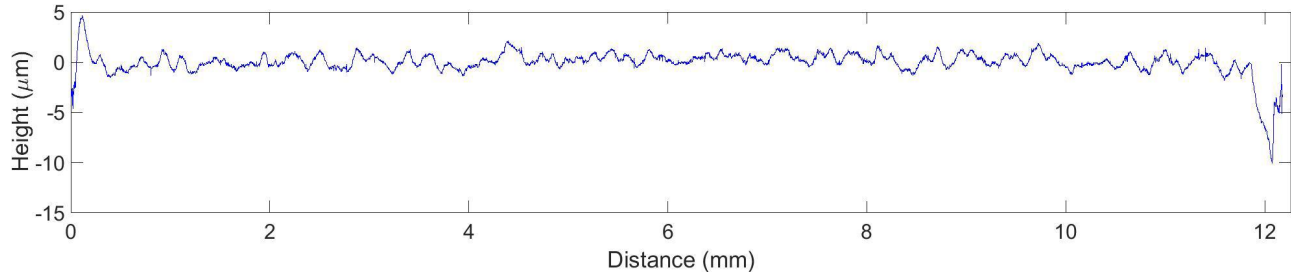
Figure 10. Surface topography measurement of the scan track. Profile was taken down the center of the scan track via laser confocal microscope.

4. COMPARISON OF MEASUREMENT TECHNIQUES

With the different methodologies for analyzing the scan track defined, a comparison of these methods can be made to determine if variations in the data from one method translate to variations in the data in another method. The data from in-situ high speed video is time based (i.e., frames/s) and the data from ex-situ measurements is spatially based (i.e., distance from the start of the scan track). However, since the frame rate of the camera and travel velocity of the experiment are known, an approximate distance down the track can be calculated using the following equation:

$$x = \frac{N \times F}{V} \, , \tag{1}$$

where x is the distance from the start of the scan track, N is the number of frames since the start of the track, F is the frame rate (30 000 frames/s in this experiment), and V is the travel velocity (800 mm/s in this experiment). A comparison of the different data sources and a highlight of features that will be investigated can be seen in Figure 11.
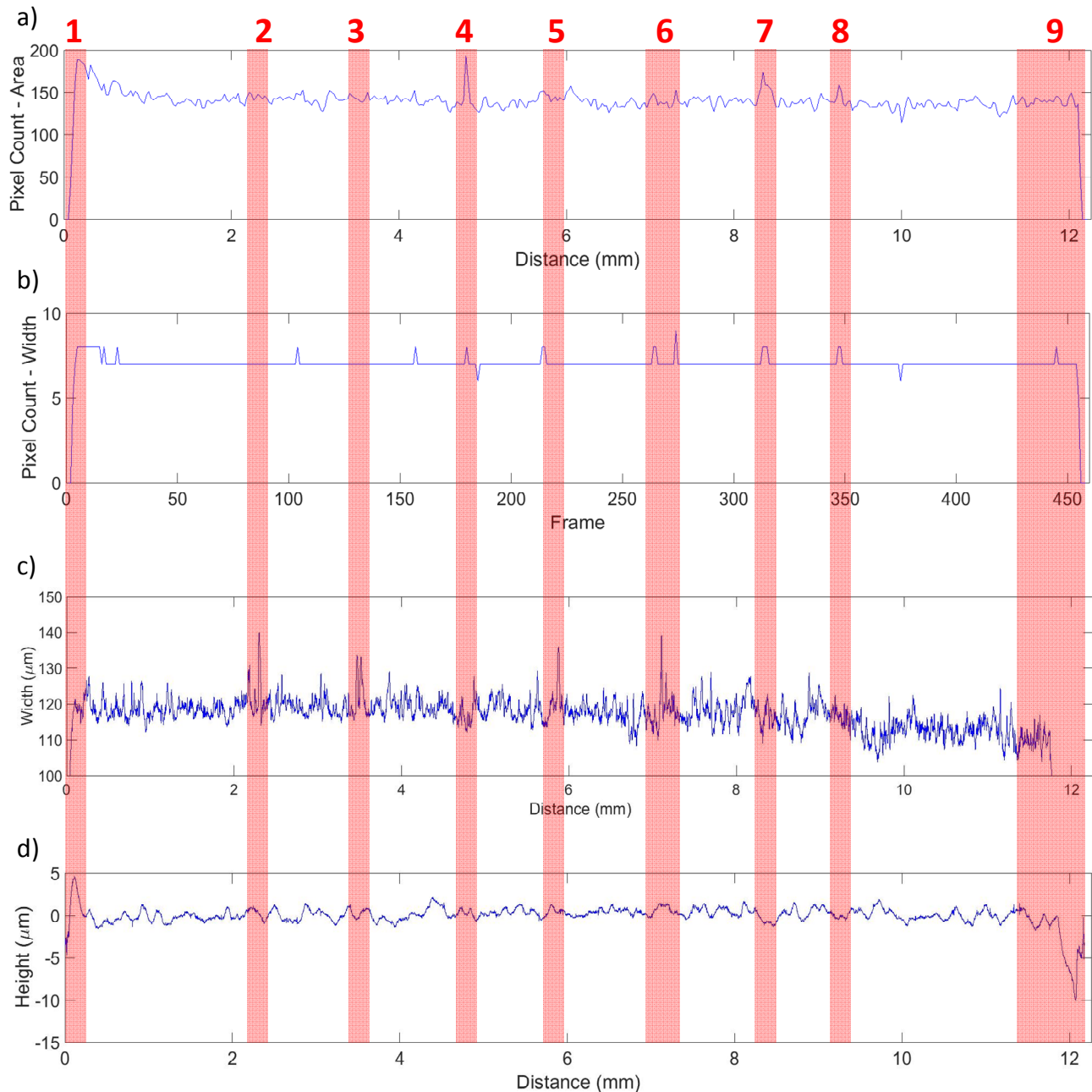
Figure 11. A comparison of the data from the in-situ high speed video with a 0.2 threshold applied depicting a) the total pixel count and b) the melt pool width pixel count, as well as ex-situ measurement of the scan track c) width and d) height. Key features in the data are denoted in red and numbered from 1 to 9.

4.1 Analysis of Feature 1

Still frames from the high-speed video, the binary conversion using a threshold level of 0.2, and measurement of area and width from the binary image can be seen in Figure 12. The data from this portion of the video shows an increase in the area and width measurements. Note that the average area for the 0.2 threshold is (139.1 ± 18.6) pixel^2.

Frame [Distance (μm)]	3 [80.0]	4 [106.7]	5 [133.3]	6 [160.0]	7 [186.7]
Area (pixels²)	39	100	160	189	186
Width (pixels)	5	7	8	8	8

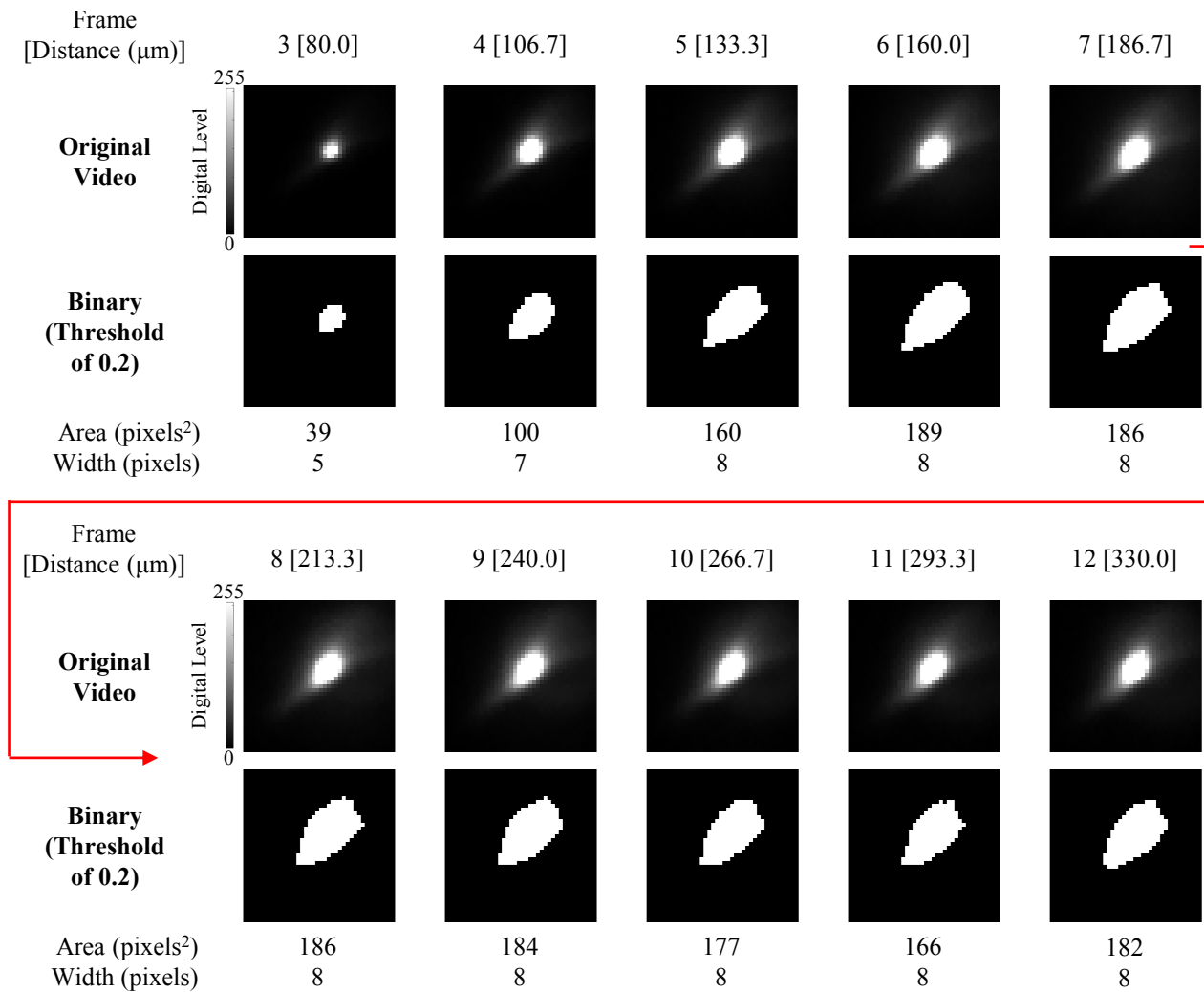| Frame [Distance (μm)]	8 [213.3]	9 [240.0]	10 [266.7]	11 [293.3]	12 [330.0]
Area (pixels²)	186	184	177	166	182
Width (pixels)	8	8	8	8	8

Figure 12. Still frames from the high-speed video representing data artifact 1, as presented in Figure 11. The size of the images presented are 40 pixels by 40 pixels. Direction of travel is previously defined in Figure 3.

Height data from start of the track, which is the location corresponding to video frames seen in Figure 12, can be seen in Figure 13. While a consolidation of material can be seen at the start of the scan track, it is not clear that this is related to the increased pixel count from the start of the video (i.e., measurements in Figure 12). This type of feature is likely due to fluid and surface tension effects in the molten metal. Prior work from Lawrence Livermore National Laboratory has shown that this type of feature is created well behind the point where the heat source is positioned on the surface [11]. Therefore, despite an apparent 'peak' at feature 1 in the camera data and surface height measurements, the physical bump and the apparent peak in brightness likely stem from two different physical phenomena.
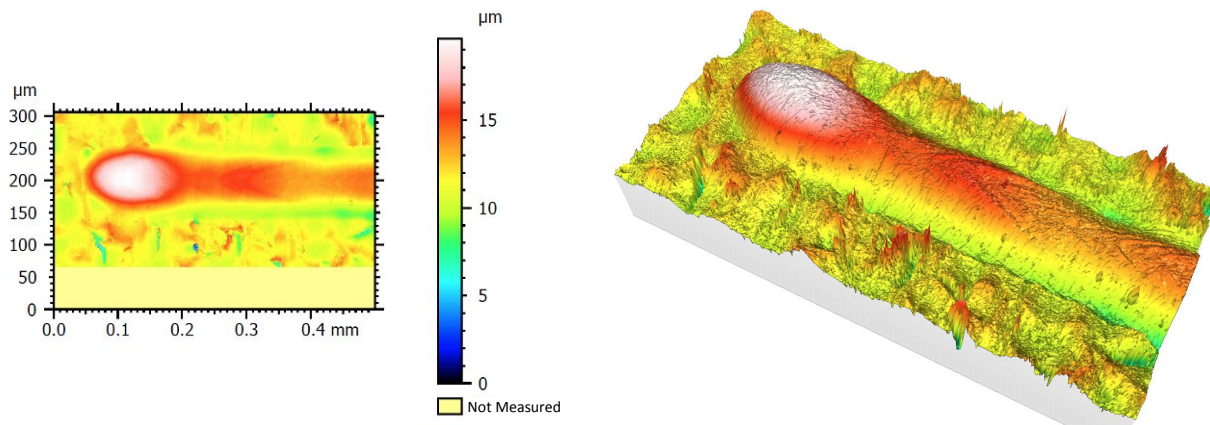
Figure 13. Height data from the scan track at a position corresponding to feature 1, which was previously described in Figure 11.

4.2 Analysis of Feature 2

An optical image of the scan track and height data near the location corresponding to feature 2 in Figure 11, can be seen in Figure 14 and matching features from the optical and topographic data have been highlighted. Interestingly, what appears to be a solidified melt droplet in the optical image shows up as a recess in the height measurement, leading to questions on the ability of optical images alone to correctly identify features. For this feature, no video stills are included as no noticeable variation in the video data was seen.
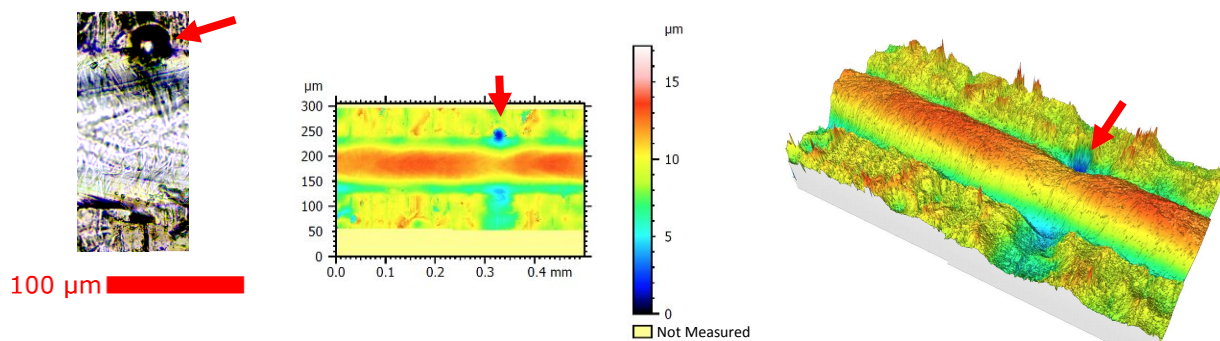

Figure 14. Optical image of the scan track and height data at a position corresponding to feature 2 described in Figure 11. Travel direction is to the right.

4.3 Analysis of Feature 3

An optical image of the scan track and height data near the location corresponding to feature 3 in Figure 11, can be seen in Figure 15 and matching features from the optical and topographic data have been highlighted. For this feature, no noticeable variation in the video data can be seen and so video stills are not included.
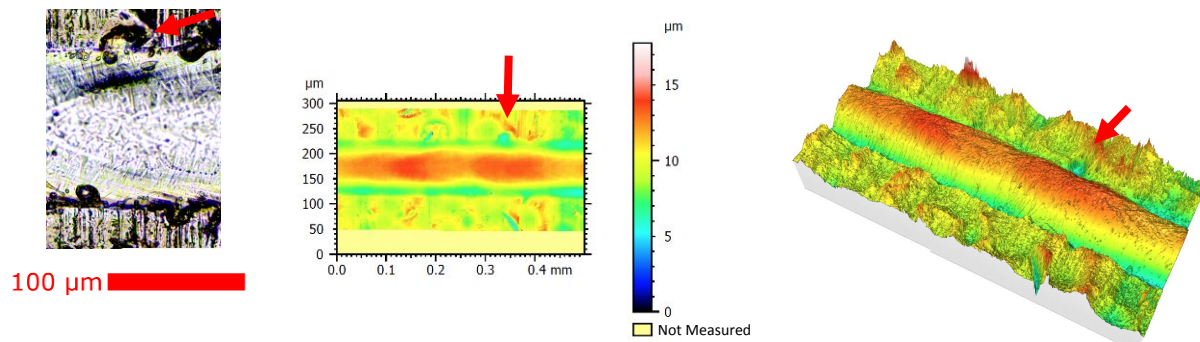
Figure 15. Optical image of the scan track and height data at a position corresponding to feature 3 described in Figure 11. Travel direction is to the right.

4.4 Analysis of Feature 4

Still frames from the high-speed video, the binary conversion using a threshold level of 0.2, and measurement of area and width from the binary image can be seen in Figure 16. The data from this portion of the video shows material being ejected from the melt pool, which is also represented as a spike in the pixel area of the binary image.

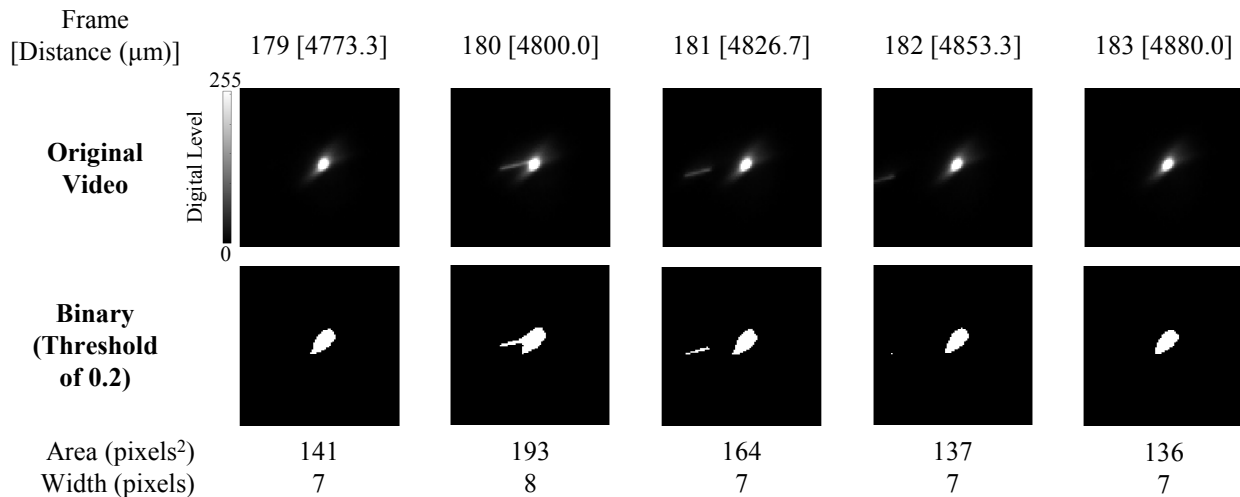| Frame [Distance (µm)]	179 [4773.3]	180 [4800.0]	181 [4826.7]	182 [4853.3]	183 [4880.0]
Area (pixels^2)	141	193	164	137	136
Width (pixels)	7	8	7	7	7

Figure 16. Still frames from the high-speed video representing feature 4, as presented in Figure 11. The size of the images presented are 100 pixels by 100 pixels. Direction of travel is previously defined in Figure 3.

An optical image of the scan track and height data near the location corresponding to feature 4 in Figure 11, can be seen in Figure 17. From these images, little variation in the surface can be seen near points of material ejecta.
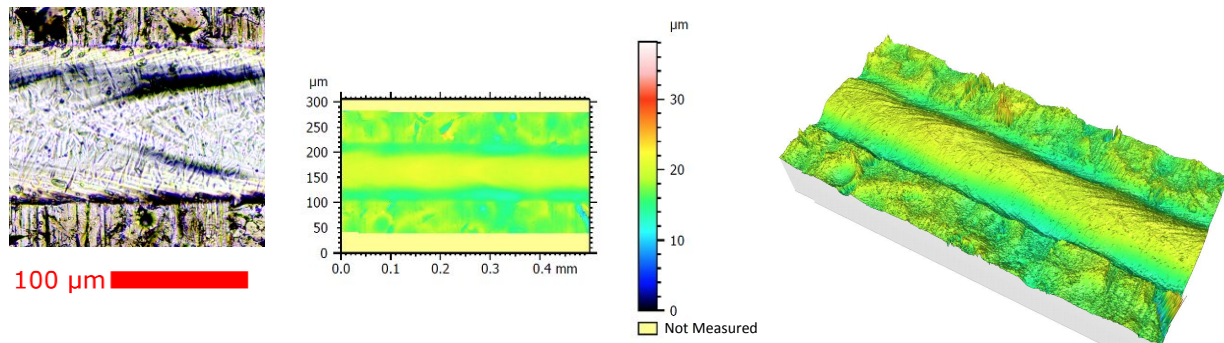
Figure 17. Optical image of the scan track and height data at a position corresponding to feature 4 described in Figure 11. Travel direction is to the right.

4.5 Analysis of Feature 5

An optical image of the scan track and height data near the location corresponding to feature 5 in Figure 11, can be seen in Figure 18. For this feature, it is difficult to match the optical image to a corresponding position in the height data as the microscope used does not provide a true color overlay onto the height data (a commercially available feature of some systems). Additionally, no noticeable variation in the video data can be seen and so video stills are not included.
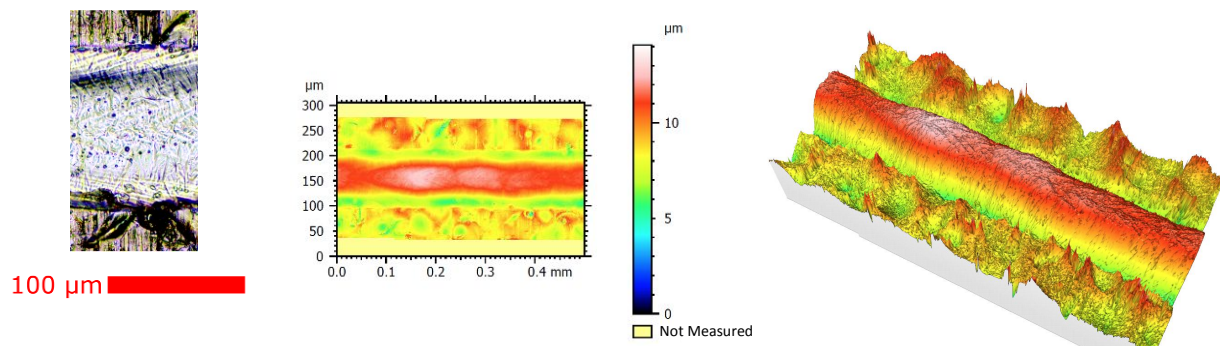

Figure 18. Optical image of the scan track and height data at a position corresponding to feature 5 described in Figure 11. Travel direction is to the right.

4.6 Analysis of Feature 6

Still frames from the high-speed video, the binary conversion using a threshold level of 0.2, and measurement of area and width from the binary image can be seen in Figure 19 and the corresponding optical image and height data can be seen in Figure 20. Video frames near this position show a glowing piece of material to the right of the melt pool in frame 274. This feature likely corresponds to the feature highlighted in the optical and topographic data in Figure 20.

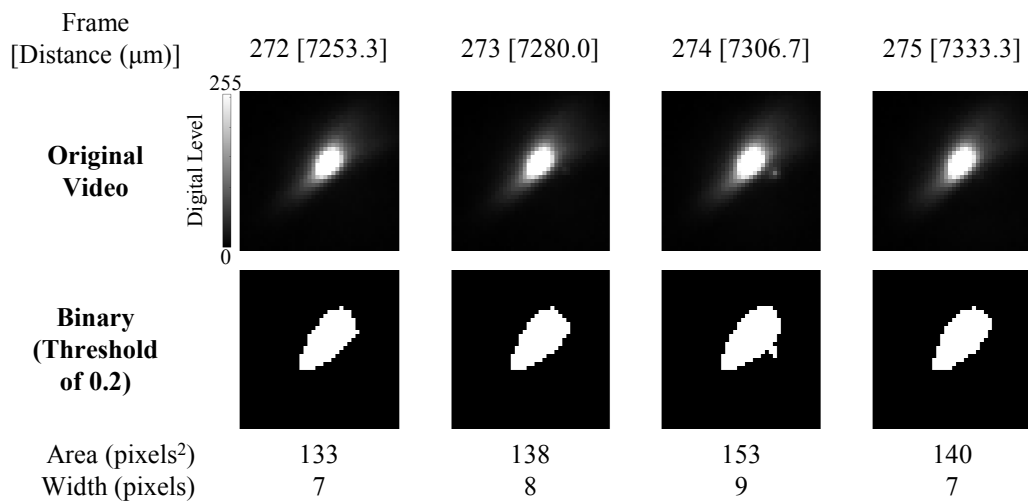| Frame [Distance (μm)]	272 [7253.3]	273 [7280.0]	274 [7306.7]	275 [7333.3]
Original Video				
Binary (Threshold of 0.2)				
Area (pixels^2)	133	138	153	140
Width (pixels)	7	8	9	7

Figure 19. Still frames from the high-speed video representing feature 6, as presented in Figure 11. The size of the images presented are 40 pixels by 40 pixels. Direction of travel is previously defined in Figure 3.
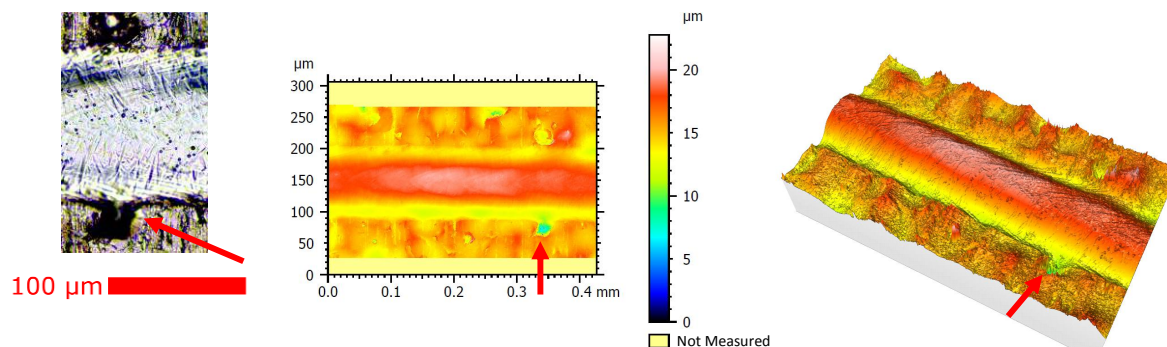

Figure 20. Optical image of the scan track and height data at a position corresponding to feature 6 described in Figure 11. Travel direction is to the right.

4.7 Analysis of Feature 7

Still frames from the high-speed video, the binary conversion using a threshold level of 0.2, and measurement of area and width from the binary image can be seen in Figure 21. The data from this portion of the video shows an increase in the size of the melt pool, which is also seen in the measured area of the binary image.

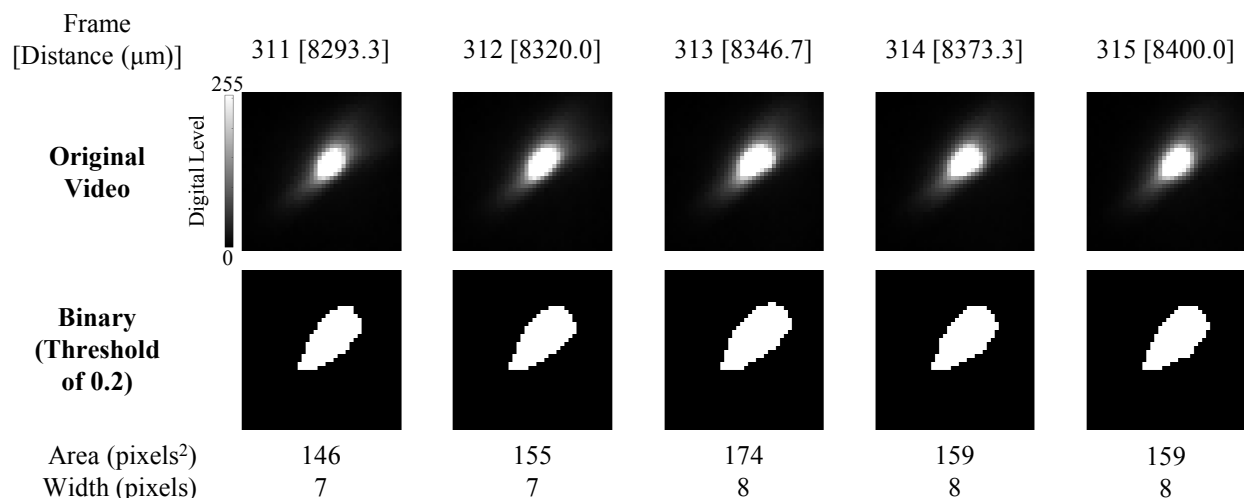| Frame [Distance (µm)]	311 [8293.3]	312 [8320.0]	313 [8346.7]	314 [8373.3]	315 [8400.0]
Original Video					
Binary (Threshold of 0.2)					
Area (pixels^2)	146	155	174	159	159
Width (pixels)	7	7	8	8	8

Figure 21. Still frames from the high-speed video representing feature 7, as presented in Figure 11. The size of the images presented are 40 pixels by 40 pixels. Direction of travel is previously defined in Figure 3.

An optical image of the scan track and height data near the location corresponding to feature 7 in Figure 11, can be seen in Figure 22. From these images, little variation in the surface can be seen to relate back to the video data in Figure 21.
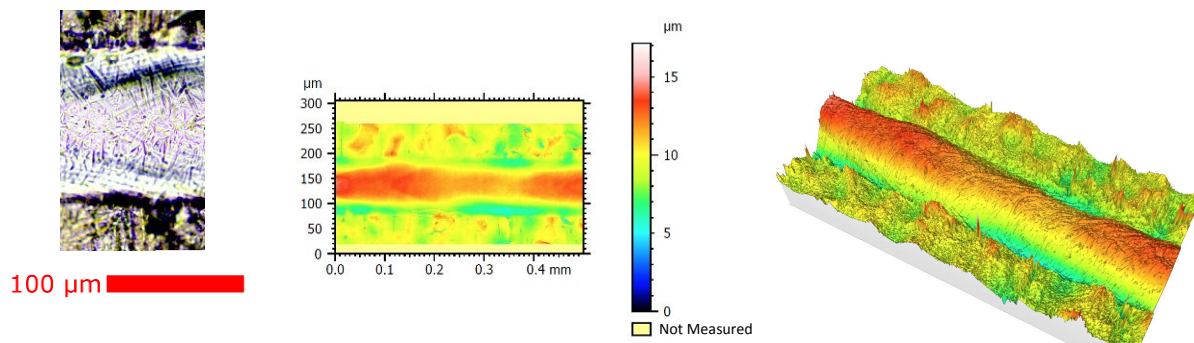

Figure 22. Optical image of the scan track and height data at a position corresponding to feature 7 described in Figure 11. Travel direction is to the right.

4.8 Analysis of Feature 8

Still frames from the high-speed video, the binary conversion using a threshold level of 0.2, and measurement of area and width from the binary image can be seen in Figure 23 and the optical image and height data from the location corresponding to video frames can be seen in Figure 24. Video frames near this position show a glowing piece of material to the right of the melt pool in frames 347 and 348. Unlike the data seen from feature 6, this feature did not have any distinct relation to the optical or height data in Figure 24.

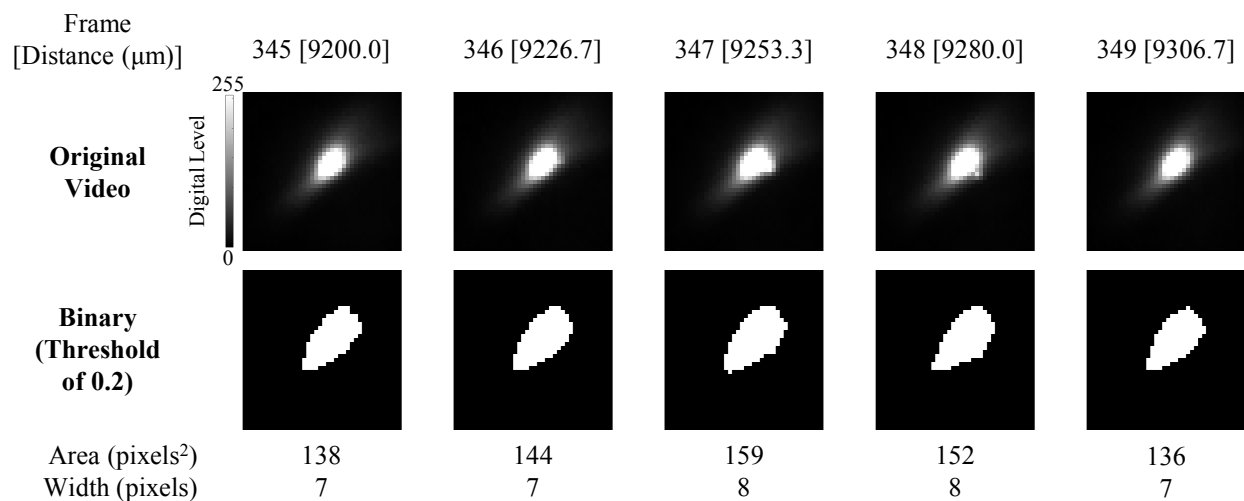| Frame [Distance (μm)]	345 [9200.0]	346 [9226.7]	347 [9253.3]	348 [9280.0]	349 [9306.7]
Original Video					
Binary (Threshold of 0.2)					
Area (pixels²)	138	144	159	152	136
Width (pixels)	7	7	8	8	7

Figure 23. Still frames from the high-speed video representing feature 8, as presented in Figure 11. The size of the images presented are 40 pixels by 40 pixels. Direction of travel is previously defined in Figure 3.
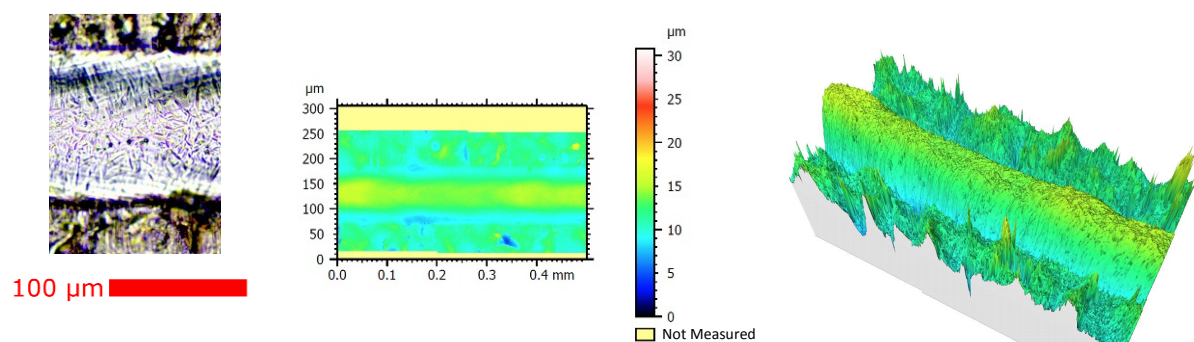

Figure 24. Optical image of the scan track and height data at a position corresponding to feature 8 described in Figure 11. Travel direction is to the right.

4.9 Analysis of Feature 9

Height data near the end of the track, corresponding to feature 9 in Figure 11, can be seen in Figure 25. At the end of the scan track, a recess can be seen showing the rapid freezing of the melt pool. There is, however, no evidence of this change from the in-situ video nor the optical width measurement, providing additional support to the conclusion that the corresponding camera data and topographic data for feature 1 do not correspond to the same physical phenomena.
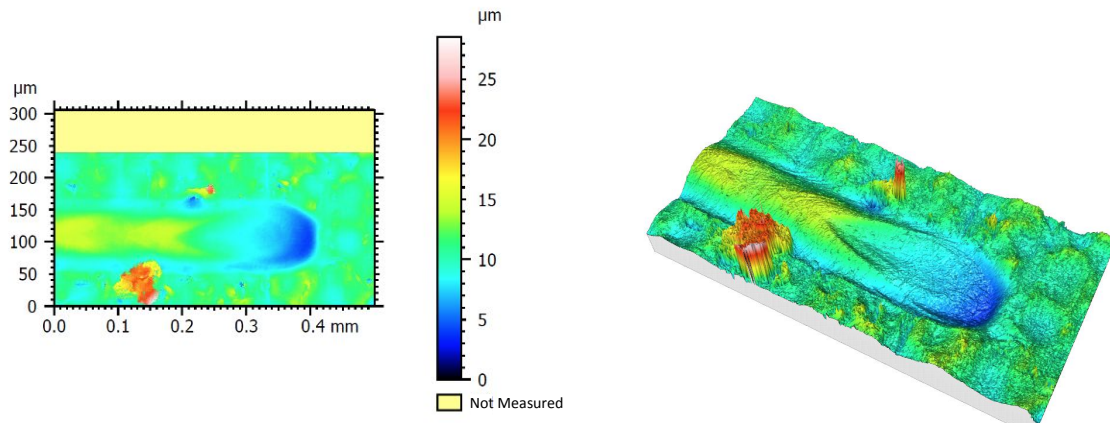
Figure 25. Height data from the scan track at a position corresponding to feature 9 described in Figure 11. Travel direction is to the right.

5. DISCUSSION

Analysis of the still frames has allowed for better characterization of the variation seen in the pixel counts, but it is clear from the data presented and analysis methods described in this paper that the signatures from in-situ and ex-situ measurements lack consistency and prevalence to determine specific correlations using the analysis methods described for this specific test case. Video data from features 1 and 7 show an increase in the overall size of the melt pool, with no clear relation to the ex-situ analysis (e.g., optical images, width measurements, or height measurements). Ex-situ measurements from features 2, 3, 5, and 9 show significant variation in the width measurement with no corresponding variation in the video data. Finally, while video data from features 6 and 8 show glowing material to the side of the melt pool, only feature 6 had corresponding variations in the ex-situ analysis.

This, however, does not prohibit additional features of interest or more advanced data analysis methods from aiding the development of these correlations. Recall that the standard deviation of the optical width measurement is only 4.3 μm, whereas the scale on the high-speed camera is 15 μm/pixel, not including effects of image blur. Thus, it is difficult to assume that any variation on this size scale can be captured through the described techniques. In addition to exploration of more advanced analysis techniques, future work will expand the experiments to include additional power and velocity combinations, the addition of powder material, and the influence of heat build-up from adjacent scan tracks. These scenarios are more indicative of a true LPBF build and are expected to create additional features typical of the process. Such features are expected to include larger variations in melt pool width and height or keyhole formation, and therefore more evidence to align the in-situ sensor signals to ex-situ scan track measurements.

6. CONCLUSIONS

A methodology for analyzing a coaxially aligned high speed NIR camera signal, monitoring a LPBF process has been presented. The analysis has been applied to an initial test case, which was performed on the AMMT prototype system at NIST, using 17-4 stainless steel. The result of the analysis has shown that, while the system can capture real-time events of the process, such as material ejecta, significant correlation between events captured by the in-situ monitoring system and features of the resultant scan track width and topography was not able to be obtained due to a limited type and frequency of observed events. As such, further analysis and experimentation is required to determine temporal and spatial locations for features of interest in the in-situ monitoring equipment and ex-situ measurement analysis.

7. ACKNOWLEDGEMENTS

REFERENCES

[1] Energetics Inc. for National Institute of Standards and Technology. "Measurement science roadmap for metal-based additive manufacturing" (2013). http://www.nist.gov/el/isd/upload/NISTAdd_Mfg_Report_FINAL-2.pdf (accessed December 15, 2014).

[2] Mazumder, J., Song, L. "Advances in Direct Metal Deposition," Proceedings of the International Mechanical Engineering Congress and Exposition (2013). doi:10.1115/IMECE2013-65042.

[3] Huang, Y., Leu, M. C., Mazumder, J., Donmez, A., "Additive Manufacturing: Current State, Future Potential, Gaps and Needs, and Recommendations," Journal of Manufacturing Science and Engineering, 137, 014001-01-014001-10 (2015). doi:10.1115/1.4028725.

[4] Spears T. G., Gold S. A., "In-process sensing in selective laser melting (SLM) additive manufacturing," Integrating Materials and Manufacturing Innovation 5, 1–25 (2016). doi:10.1186/s40192-016-0045-4.

[5] Grasso, M., Colosimo, B. M. "Process defects and in situ monitoring methods in metal powder bed fusion: a review," Meas Sci Technol (2017), 28:044005. doi:10.1088/1361-6501/aa5c4f.

[6] Berumen, S., Bechmann, F., Lindner, S., Kruth, J. P., Craeghs, T., "Quality control of laser- and powder bed-based Additive Manufacturing (AM) technologies," Phys Proc 5, Part B,617–22 (2010). doi:10.1016/j.phpro.2010.08.089.

[7] Grantham, S., Lane, B., Neira, J., Mekhontsev, S., Vlasea, M., Hanssen, L., "Optical design and initial results from NIST's AMMT/TEMPS facility," Proc. SPIE 9738, p. 97380S–97380S–9 (2016). doi:10.1117/12.2214246.

[8] Lane, B., Mekhontsev, S., Grantham, S., Vlasea, M.L., Whiting, J., Yeung, H., Fox, J. C., et al., "Design, Developments, and Results from the NIST Additive Manufacturing Metrology Testbed (AMMT)," Proceedings of the 26th Annual International Solid Freeform Fabrication Symposium – An Additive Manufacturing Conference, Austin, TX, p. 1145–60 (2016).

[9] Heigel, J. C., Lane, B. M., "Measurement of the Melt Pool Length During Single Scan Tracks in a Commercial Laser Powder Bed Fusion Process," Proceedings of the ASME 2017 12th International Manufacturing Science and Engineering Conference, Los Angeles, CA, USA (2017).

[10] Lane, B., Moylan, S., Whitenton, E. P., Ma, L., "Thermographic measurements of the commercial laser powder bed fusion process at NIST," Rapid Prototyping Journal 22,778–87 (2016). doi:10.1108/RPJ-11-2015-0161.

[11] Fox, J. C., Lopez, F. F., Lane, B. M., "On the Requirements for Model-Based Thermal Control of Melt Pool Geometry in Laser Powder Bed Fusion Additive Manufacturing," Proceedings of the 2016 Material Science & Technology Conference, Salt Lake City, UT (2016).

[12] Khairallah, S. A., Anderson, A. T., Rubenchik, A., King, W. E., "Laser powder-bed fusion additive manufacturing: Physics of complex melt flow and formation mechanisms of pores, spatter, and denudation zones," Acta Materialia 108,36–45 (2016). doi:10.1016/j.actamat.2016.02.014.